Flow (2025), **5** E12
doi:10.1017/flo.2025.8

FLOW CAMBRIDGE UNIVERSITY PRESS

RESEARCH ARTICLE

Regulating nanofibril assembly using diverse flow-focusing channels

Kosuke Osawa[1], V. Krishne Gowda[2,3], Tomas Rosén[4,5,6], Stephan V. Roth[4,7], L. Daniel Söderberg[4,5,6], Junichiro Shiomi[1,8] and Fredrik Lundell[2,3,5,6]

[1]Mechanical Engineering, University of Tokyo, Tokyo, Japan
[2]Engineering Mechanics, KTH Royal Institute of Technology, Stockholm, Sweden
[3]FLOW, KTH Royal Institute of Technology, Stockholm, Sweden
[4]Fibre and Polymer Technology, KTH Royal Institute of Technology, Stockholm, Sweden
[5]Wallenberg Wood Science Center, KTH Royal Institute of Technology, Stockholm, Sweden
[6]Treesearch, KTH Royal Institute of Technology, Stockholm, Sweden
[7]Deutsches Elektronen-Synkrotron DESY, Hamburg, Germany
[8]Institute for Engineering Innovation, University of Tokyo, Tokyo, Japan
Corresponding author: Fredrik Lundell; Email: fredrik@mech.kth.se

Received: 30 September 2024; **Revised:** 16 February 2025; **Accepted:** 24 February 2025

Keywords: assembly; cellulose nanofibrils; flow-focusing; X-ray scattering; rotary diffusion

Abstract

Properties and functions of materials assembled from nanofibrils critically depend on alignment. A material with aligned nanofibrils is typically stiffer compared with a material with a less anisotropic orientation distribution. In this work, we investigate nanofibril alignment during flow focusing, a flow case used for spinning of filaments from nanofibril dispersions. In particular, we combine experimental measurements and simulations of the flow and fibril alignment to demonstrate how a numerical model can be used to investigate how the flow geometry affects and can be used to tailor the nanofibril alignment and filament shape. The confluence angle between sheath flow and core flow, the aspect ratio of the channel and the contractions in the sheath and/or core flow channels are varied. Successful spinning of stiff filaments requires: (i) detachment of the core flow from the top and bottom channel walls and (ii) a high and homogeneous fibril alignment. Somewhat expected, the results show that the confluence angle has a relatively small effect on alignment compared with contractions. Contractions in the sheath flow channels are seen to be beneficial for detachment, and contractions in the core flow channel are found to be an efficient way to increase and homogenise the degree of alignment.

Impact Statement

In the context of sustainability, circular material systems require the development of alternatives to fossil-based and energy-consuming materials. One attractive path is less-energy-demanding materials made from biobased resources. Many natural materials obtain impressive properties by a hierarchical structure, where nanosized subassemblies appear in a structured manner. In this work, we combine experimental and numerical work to demonstrate how different channel flow geometries can be used to organise the most abundant of such subassemblies, cellulose nanofibrils, in aligned structures. The aligned structures can, after further processing such as gelation and drying, develop into high-performance engineering materials.

1. Introduction

Dispersed particles of micrometric (10^{-6} m) and nanometric (10^{-9} m) size are ubiquitous in the biological world, and are promising building blocks for developing sustainable, biocompatible materials (Solomon & Spicer 2010). A few examples are biopolymers and colloids such as cellulose nanofibrils (CNFs) in trees, algae and bacteria (Moon *et al.* 2011), chitin nanofibrils in animals (Ehrlich 2010), silk nanofibrils from spiders and silkworms (Ling *et al.* 2017), protein nanofibrils from eggs (Humblet-Hua *et al.* 2008) and milk (Loveday *et al.* 2012) and viruses like tobaccomosaic virus (Nemoto *et al.* 1975) or coronavirus (Kanso *et al.* 2020).

Amongst these, CNFs (diameter ranging from 2 to 100 nm) are of particular interest, since they are lightweight, available in abundance, renewable and biocompatible, and have high mechanical performance (Ling, Kaplan & Buehler 2018; Li *et al.* 2021). With control of their hierarchical structure, nanofibrils have been used in the fabrication of macroscopic materials ranging from macrofibres (Iwamoto, Isogai & Iwata 2011) and composites (Capadona *et al.* 2007) to thin films (Lagerwall *et al.* 2014), porous membranes and gels (Håkansson *et al.* 2016). Thus, as renewable, biocompatible building blocks, CNFs can be a key ingredient for circular material systems.

One assembly technology that has shown great potential for controlling and regulating nanofibril assembly is hydrodynamic assembly (Nunes *et al.* 2013; Hou *et al.* 2017). A method of particular interest is flow focusing (Anna, Bontoux & Stone 2003), which is illustrated in figure 1. Here, a core flow of nanofibril colloidal dispersion is focused by its own solvent through outer sheath flows, to first align fibrils, and then use colloidal chemistry to lock them in a gel thread that can be dried into a filament (Håkansson *et al.* 2014; Kamada *et al.* 2017). The properties of the assembled nanofibril filaments (e.g. stiffness, strength and biological and electrical functions) are, to a large extent, determined by the alignment of the fibrils. By controlling the alignment and orientation of nanofibrils in the dispersion (Doi & Edwards 1988; Jeffery 1922; Tucker III 2022), these nanofibril filaments could indeed form the foundation for sustainable material technologies. Engineering sustainable materials from natural building blocks of colloidal particles (e.g. cellulose or protein nanofibrils) using microfluidic flows requires an in-depth understanding of the behaviour of colloidal particle dispersions under flowing conditions (Calabrese, Shen & Haward 2023).

In order to achieve successful assembly and alignment of fibrils, the flow must be tuned to form a thread, and there must be extensional or sheared flow that aligns the fibrils. In a combined numerical and experimental study of the flow in the geometry of figure 1(*a*), Gowda *et al.* (2019) showed (i) that a crucial aspect for good thread formation is Korteweg stresses (Korteweg 1901) in regions of concentration gradients, which give rise to an effective interfacial tension (EIT) between the colloidal dispersion in the core and its solvent in the sheath flows (Truzzolillo *et al.* 2015), and (ii) that if the EIT is introduced in computational fluid dynamic simulations, an excellent agreement is obtained between the simulated flow fields and experimental measurements acquired with optical coherence tomography. In a follow-up study, Gowda *et al.* (2021) further demonstrated the accuracy of the numerical flow model for all geometries of figure 1(*a–e*), where the confluence angle β between the core and sheath flows is varied between 30° and 150°.

For fibril alignment, the numerical flow fields were used as input to alignment simulations based on a Smoluchowski equation for the orientation distribution function (Doi & Edwards, 1988; Tucker III, 2022), and it was shown that the alignment observed by small-angle X-ray scattering (SAXS) measurements in the first geometry ($\beta = 90°$; figure 1*a*) could be reproduced by a two-fraction model (Gowda *et al.* 2022). This two-fraction model is a coarse approximation of the actual dispersion, but it was found to be sufficient for approximating the continuous length distribution of the fibrils.

In this work, we expand on previous work and gain insights into how flow geometry affects thread formation and fibril alignment. First, a brief summary of the methods used is given in § 2. Four sets of results are presented in § 3. The first set is a comparison between numerical and experimental alignment data for the geometries with confluence angles $\beta = 90°$, 60° and 120° (figure 1*a–c*). In the second set of results, the numerical alignment model is used to compare fibril alignment for all five confluence

https://doi.org/10.1017/flo.2025.8 Published online by Cambridge University Press

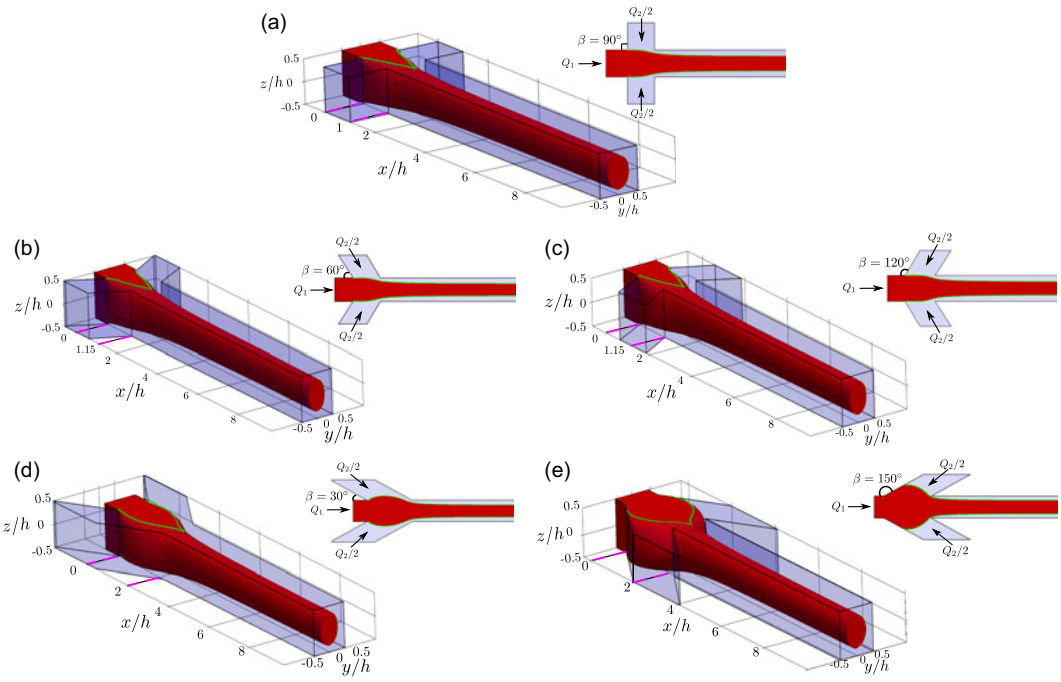

Figure 1. *(a–e) Schematic illustration of various flow-focusing geometries. As seen from the top views, the side inlet channel arms join the main central channel at a confluence angle β varying between $30°$ and $150°$. The core fluid, denoted by red colour, enters the main central inlet channel arm with a volumetric flow rate Q_1. The sheath fluid, represented by light-blue colour, enters from the side inlet channel arms with a flow rate of $Q_2/2$ from each side. The cross-section of the central channel arm in all these geometrical configurations is square with sidelength h.*

angle geometries. The third set is a numerical study of the flow in eight new flow geometries where the channel aspect ratio is varied and/or contractions are added in the core and/or sheath-flow channels. The fourth and final set of results uses the simulated flow in the eight new geometries to investigate thread formation and fibril alignment. The mean alignment at each streamwise position and the variation over the channel cross-section are evaluated. Finally, the conclusions are summarised in § 4.

2. Numerical and experimental methods

2.1. Flow modelling

The methods of the present study build on previous works (Gowda *et al.* 2019; Gowda *et al.* 2022) as summarised schematically in figure 2(*a*). The flow is modelled as a two-phase flow with a sharp interface in open-source computational fluid dynamic code OpenFOAM (Weller *et al.* 1998), where the rheology of the inner (core fluid) and outer (sheath fluid) flows is determined by rheometry measurements. The volumetric flow rates (see figure 1) are $Q_1 = 6.5$ mm^3 s^{-1} for the core flow and $Q_2 = 7.5$ mm^3 s^{-1} for the two sheath flows together.

Figure 2(*b*) shows the rheology flow curves for the core and sheath fluids. The viscosity of the core fluid CNF dispersion, η_1, is described by the non-Newtonian Carreau model:

$$\eta_1 = \eta_{\inf} + (\eta_0 - \eta_{\inf})[1 + (\tau\dot{\gamma})^2]^{(n-1)/2}. \tag{2.1}$$

where $\eta_{\inf}$ is the infinite shear viscosity, η_0 the zero-shear viscosity, τ the relaxation time, $\dot{\gamma}$ the shear rate and n the power index. The parameters of the Carreau model (solid black line in figure 2*b*) are:

https://doi.org/10.1017/flo.2025.8 Published online by Cambridge University Press

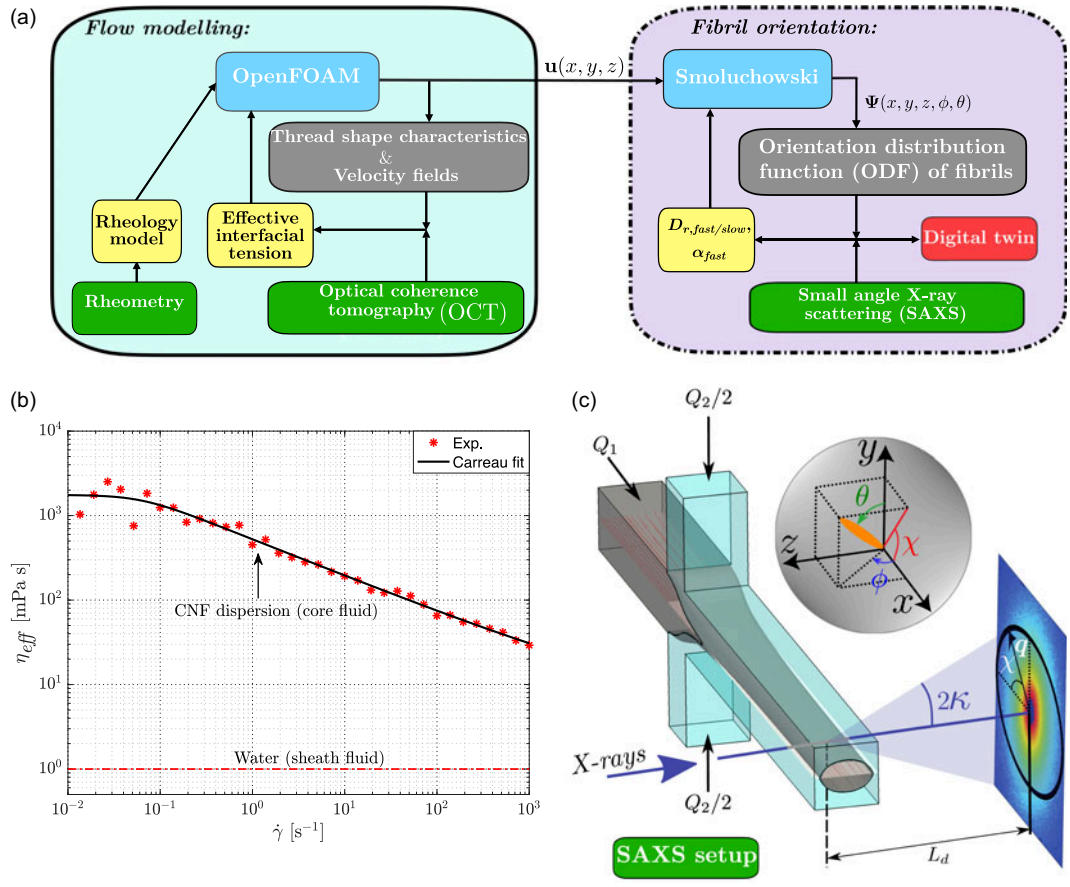

Figure 2. *(a) Schematic illustration of the connection between flow modelling simulations and fibril orientation. Green blocks denote the experimental methods: rheometry, optical coherence tomography and SAXS. Yellow blocks indicate the variables used to calibrate the flow and fibril orientation numerical models represented by blue blocks. Grey blocks show the output features used for comparing experimental measurements and numerical model results. Red block indicates the digital twin developed through fibril orientation modelling. Velocity fields* $\boldsymbol{u}(x, y, z)$ *obtained from flow modelling are the main input to fibril orientation modelling. (b) Shear viscosity measurements of core and sheath fluids. Red markers show the measured rheology of the CNF dispersion used in the present work, modelled using a non-Newtonian Carreau rheology model (equation (2.1)). The solid black line represents the Carreau fit, while the dash-dotted red line shows the viscosity of sheath fluid water. (c) Illustration of SAXS set-up. An X-ray beam traverses the flow-focusing geometry along the* x *and* y *directions, and the resulting projected scattering image is captured by a two-dimensional detector placed at a distance of* L_d *from the flow-focusing channel. The Cartesian coordinate system* x, y, z *and the fibril orientation angles* ϕ *and* θ *in spherical coordinates and/or the projected orientation angle* χ *describe the orientation of fibrils, statistically described by orientation distribution functions* Ψ*.*

$\eta_{\inf} = 5$ mPa s, $\eta_0 = 1756$ mPa s, $\tau = 16.16$ s and $n = 0.56$. The viscosity of the sheath fluid (water) is $\eta_2 = 1$ mPa s.

The system of equations solved with OpenFOAM are the Navier–Stokes equation:

$$\frac{\partial \rho \mathbf{u}}{\partial t} + \nabla \cdot (\rho \mathbf{u}\mathbf{u}) = -\nabla P + \nabla \cdot \mathrm{T} + \rho \boldsymbol{g} + \boldsymbol{f_s}, \tag{2.2}$$

https://doi.org/10.1017/flo.2025.8 Published online by Cambridge University Press

the continuity equation:

$$\nabla \cdot \mathbf{u} = 0 \tag{2.3}$$

and the equation for the advection of fluid fraction φ:

$$\frac{\partial \varphi}{\partial t} + \nabla \cdot (\varphi \mathbf{u}) = 0, \tag{2.4}$$

where $\mathbf{u}$ is the velocity vector field, P is the pressure and $T = 2\eta E - 2\eta(\nabla \cdot \mathbf{u})I/3$ is the deviatoric stress tensor with E as the rate of deformation tensor (the symmetric part of the velocity gradient tensor) and I as the identity matrix. The fluid fraction φ varies smoothly between 0 and 1, such that $\varphi = 0$ for the core fluid and $\varphi = 1$ for the sheath fluid. The body force per unit volume $\boldsymbol{f_s}$ is localised to the interface between the core and sheath fluids as defined below and accounts for the surface tension forces.

The bulk parameters density ρ and viscosity η are computed based on the weighted average distribution of the fluid fraction φ:

$$\rho = \rho_1 \varphi + \rho_2 (1 - \varphi), \tag{2.5}$$

$$\eta = \eta_1 \varphi + \eta_2 (1 - \varphi), \tag{2.6}$$

where $\rho_1, \rho_2, \eta_1, \eta_2$ are the densities and the viscosities of the two fluids. The surface tension force $\boldsymbol{f_s}$ is modelled as a volumetric force using the continuum surface force method (Brackbill, Kothe & Zemach 1992), and is defined as

$$\boldsymbol{f_s} = \gamma \kappa \nabla \varphi, \tag{2.7}$$

where φ is the fluid fraction, γ the interfacial tension and κ the local curvature of the interface determined by

$$\kappa = -\nabla \cdot \left(\frac{\nabla \varphi}{|\nabla \varphi|} \right). \tag{2.8}$$

In addition to the complex rheology, the dynamics of the physical flow system is controlled by an ultralow EIT of $O(10^{-4}–10^{1})$ mN m^{-1} (Truzzolillo *et al.* 2015, 2016). As indicated by its name, the effect of the EIT resembles the effects of interfacial tension. The EIT models the Korteweg stresses (Korteweg 1901) that appear due to the fibril concentration gradient between the CNF dispersion (core fluid) and its solvent (sheath fluid) (Atencia & Beebe 2005; Joseph & Renardy 1993). For the present combination of CNF dispersion–solvent fluid pair, an extensive comparison between experimental and numerical flow data (Gowda *et al.* 2019) found that the flow modelling reproduces the experimental flow characteristics when $\gamma = 0.054$ mN m^{-1}. The significance of EIT on the flow dynamics of miscible co-flowing fluids was further demonstrated recently by Carbonaro *et al.* (2025).

In our previous works (Gowda *et al.* 2019; Gowda *et al.* 2021), we have thoroughly evaluated and demonstrated that the flow model described above reproduces the experimental flow features with very good agreement in terms of three-dimensional (3-D) flow topology and velocity fields as measured by optical coherence tomography.

2.2. Fibril orientation

The Smoluchowski equation (Hyensjö & Dahlkild 2008) describing the evolution of the orientation distribution Ψ of monodisperse non-spherical particles is written as

$$\begin{aligned} \frac{\mathrm{D}\Psi(\phi,\theta)}{\mathrm{D}t} = \frac{1}{\sin\theta} \Bigg[\frac{\partial}{\partial \phi} \Bigg(D_r \frac{1}{\sin\theta} \frac{\partial \Psi}{\partial \phi} - \sin\theta \dot{\phi} \Psi \Bigg) + \\ + \frac{\partial}{\partial \theta} \left(D_r \sin\theta \frac{\partial \Psi}{\partial \theta} - \sin\theta \dot{\theta} \Psi \right) \Bigg], \end{aligned} \tag{2.9}$$

where $\mathrm{D}/\mathrm{D}t$ is the material derivative following the fluid, D_r is the Brownian rotary diffusion coefficient and $\dot{\theta}$ and $\dot{\phi}$ are the rotational velocities of the particle based on the velocity gradients of the flow, the

https://doi.org/10.1017/flo.2025.8 Published online by Cambridge University Press

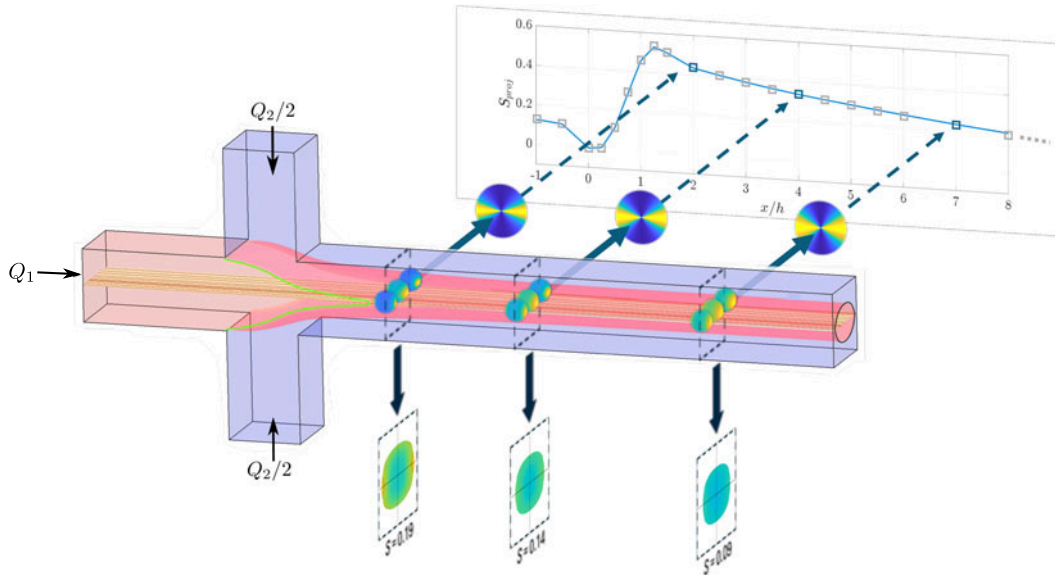

Figure 3. *Illustration of evolution of 3-D nanofibril orientation distribution Ψ along the channel length at different downstream x/h positions. The mean order parameter S and the projected order parameter S_{proj} are obtained from the average of cross-sectional local order S_{local} (equation (2.13)) and projected orientation (equation (2.14)) distributions, respectively.*

dot denoting temporal derivative. The rotational velocities are obtained from the rate of change of the director of a particle $\mathbf{p}$, defined as

$$\mathbf{p} = \begin{bmatrix} \sin\theta\cos\phi \\ \cos\theta \\ \sin\theta\sin\phi \end{bmatrix}. \tag{2.10}$$

Assuming ellipsoidal particles and the flow to be very viscous (Stokes), the rate of change of $\mathbf{p}$ (Doi & Edwards 1988; Jeffery 1922) in the local flow field is given by

$$\dot{\mathbf{p}} = W\mathbf{p} + \frac{r_p^2 - 1}{r_p^2 + 1}\left[E\mathbf{p} - (\mathbf{p}^T E\mathbf{p})\mathbf{p}\right] \tag{2.11}$$

via a projection on the unit vectors of the spherical coordinates, i.e.

$$\dot{\phi} = \dot{\mathbf{p}} \cdot \mathbf{e}_\phi, \quad \dot{\theta} = \dot{\mathbf{p}} \cdot \mathbf{e}_\theta, \tag{2.12}$$

where E and W are the symmetric (rate of deformation) and antisymmetric (vorticity) parts of the velocity gradient tensor obtained from flow modelling. The parameter r_p is the aspect ratio of the particle; $r_p > 1$ for prolate (cucumber-like) and $r_p < 1$ for oblate (pancake-like) particles. For the fibrils in the present work, $r_p > 25$ and $(r_p^2 - 1)/(r_p^2 + 1) \approx 1$. Equations (2.11)–(2.12) describe the coupling between particle rotation and velocity gradients of flow assuming that the particles are stiff and straight rod-like.

Further, the 3-D orientation distributions Ψ of the particles can be quantified through a variable called the mean order parameter S, where $S = 1$ represents an anisotropic distribution and $S = 0$ corresponds to isotropic distribution, i.e. random orientation. The order parameter can be evaluated in two ways as illustrated schematically in figure 3. The first is by calculating the local order parameter S_{local} as (Doi & Edwards 1988)

$$S_{\text{local}} = \int_A \frac{3}{2}\left[(\mathbf{e}_x \cdot \mathbf{p})^2 - \frac{1}{3}\right]\Psi \, \mathrm{d}A, \tag{2.13}$$

https://doi.org/10.1017/flo.2025.8 Published online by Cambridge University Press

where $\mathbf{e}_x$ is the unit vector in the streamwise x direction and the integration is made over the unit sphere. The mean order parameter S is the average of the local order parameter S_{local} over the cross-section. The second is the projected order parameter S_{proj} based on the projected mean orientation distribution $\Psi_{\text{proj}}(\chi)$ and is calculated as

$$S_{\text{proj}} = \int_0^{\pi} \Psi_{\text{proj}}(\chi) \left(\frac{3}{2}\cos^2\chi - \frac{1}{2}\right) \sin\chi \, \mathrm{d}\chi, \tag{2.14}$$

where Ψ_{proj} is normalised according to

$$\int_0^{\pi} \Psi_{\text{proj}}(\chi) \sin\chi \, \mathrm{d}\chi = 1. \tag{2.15}$$

Note that $-0.5 \leq S_{\text{proj}} \leq 1$, where the low and high extremes indicate that all fibrils are oriented normal and parallel to the flow direction, respectively.

The total variation of the local order parameter (S_{local}) over the cross-section is measured by the standard deviation at each streamwise position and is denoted as ΔS.

Using the numerical method and two-fraction model described in Gowda *et al.* (2022), the Smoluchowski equation (equation (2.9)) for the 3-D orientation distribution Ψ is solved along streamlines as depicted in figure 3. The Smoluchowski equation uses the flow gradients from flow modelling (see figure 2*a*) as an input together with rotary diffusion(s) D_r. In previous work on CNF alignment in flows (Gowda *et al.* 2022), it was found that a two-fraction model, where one fraction (α_{fast}) of the dispersion was assumed to have a high $D_{r,\text{fast}}$ and the other $(1-\alpha_{\text{fast}})$ a low $D_{r,\text{slow}}$, could reproduce the projected order parameter S_{proj} (see below) obtained from SAXS measurements.

As mentioned in the introduction, the two-fraction model is a coarse approximation of the actual continuous distribution originating from the length distribution of the fibrils (Brouzet *et al.* 2018). In the present context, increasing the number of fractions above two does not add to the prediction accuracy. Furthermore, with more than two fractions, the objective function (integrated difference between measured and modelled projected order parameter) does not have a distinct minimum and unique values of model parameters are not obtained.

2.3. Cellulose nanofibril dispersion

The core fluid is a 0.3 % by weight dispersion of CNFs in water. The fibrils have a diameter ranging from 2 to 6 nm, and a length distribution ranging from 100 to 1500 nm. This kind of dispersion is of special interest since it has been used to assemble and fabricate very strong cellulose filaments (Håkansson *et al.* 2014; Mittal *et al.* 2018). The rheological characterisation of the dispersion was performed with steady shear viscosity measurements. As seen from figure 2*b*, the dispersion displays a shear-thinning rheological behaviour, described by the non-Newtonian Carreau model (equation (2.1)).

2.4. Small-angle X-ray scattering

The fibril orientation in the flow-focusing configurations is quantified experimentally through SAXS measurements. The SAXS experiments were performed at the P03 beamline (Buffet *et al.* 2012) of the PETRA III Synchrotron facility at Deutsches Elektronen-Synchrotron (DESY) in Hamburg, Germany.

An X-ray beam of size 24 μm $\times$ 11 μm having a wavelength $\lambda = 0.95$ Å traverses the flow-focusing channel in x and y directions, as illustrated pictorially in figure 2*c*. The X-ray intensity scattered by the flowing colloidal fibril dispersion is recorded on the detector (Pilatus 1M, Dectris, having a pixel size of 172 μm $\times$ 172 μm), positioned at a distance of $L_d = 7.5$ m from the flow-focusing channel assembly. The magnitude of the scattering vector q is given by $q = (4\pi/\lambda)\sin\kappa$. The angle between incident and scattered light is 2κ (see figure 2*c*). The background scattering intensities were removed using scattering intensities obtained with the scans of deionised water.

https://doi.org/10.1017/flo.2025.8 Published online by Cambridge University Press

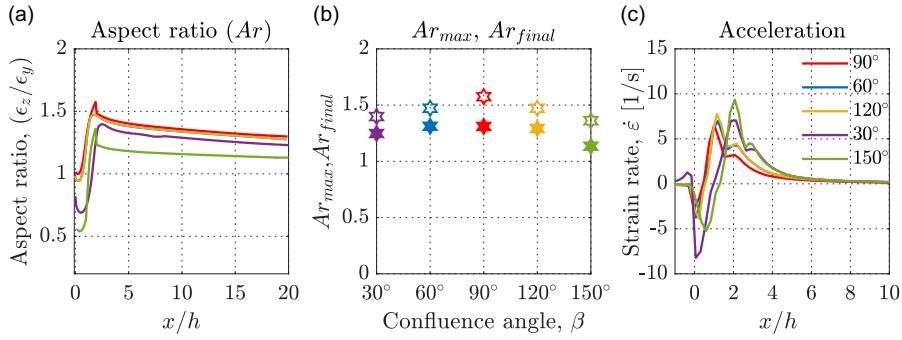

Figure 4. *(a) Development of thread aspect ratio (ϵ_z/ϵ_y) as a function of downstream x/h positions for different confluence angle β geometries. (b) Maximum (Ar_{max}, open ☆ symbols) and final (Ar_{final}, filled ★ symbols) thread aspect ratio versus the confluence angle β. (c) Evolution of strain rate $\dot{\varepsilon}$ along the centreline as a function of downstream positions x/h for different geometries.*

The orientation distribution Ψ of the nanofibrils in the scattered SAXS diffractograms is quantified with order parameter S (Van Gurp 1995) written as

$$S = \left\langle \frac{3}{2}\cos^2\chi - \frac{1}{2} \right\rangle, \tag{2.16}$$

where $\langle\cdot\rangle$ indicates an ensemble average of the particles. If all the nanofibrils are aligned with the flow direction, the order parameter $S = 1$. For an isotropic distribution, i.e. random orientation, $S = 0$. Further, as seen from figure 2*c*, the SAXS pattern captured by the two-dimensional detector along the beam path represents the projected mean orientation distribution $\Psi_{\text{proj}}(\chi)$, and the projected order parameter S_{proj} is obtained according to equations (2.14) and (2.15).

3. Results and discussion

3.1. Effect of confluence angle

3.1.1. Flow topology and flow fields

The flow in all confluence angles β from 30° to 150° (see figure 1*a–e*) was studied numerically and experimentally by Gowda *et al.* (2021). The agreement between numerical and experimental results was excellent. In figure 4, the results are summarised in terms of aspect ratio ϵ_z/ϵ_y of the core fluid thread, where ϵ_y and ϵ_z are the dimensions of the thread in the y and z directions, respectively, and acceleration (strain rate $\dot{\varepsilon}$) as a function of downstream x/h positions, as well as maximum $Ar_{\max}$ and final Ar_{final} thread aspect ratio. As the confluence angle β deviates from 90°, the aspect ratio decreases towards a circular cross-section and the acceleration increases. A somewhat surprising observation is that the results, to a large extent, are symmetric so that the aspect ratio development and flow acceleration are very similar for each of the two pairs $\beta = (60°, 120°)$ and $\beta = (30°, 150°)$.

3.1.2. Fibril alignment: comparison between experiments and simulations

First, the comparisons between alignment simulations and experiments are extended from the confluence angle $\beta = 90°$ studied by Gowda *et al.* (2022) to $\beta = 60°$ and 120° geometries, as shown in figure 5(*a–c*). The experimental order parameters from SAXS measurements were deduced using two datasets in the case of $\beta = 90°$, and one each from $\beta = 60°$ and $\beta = 120°$. In all cases, the projected order parameter S_{proj}, where $S_{\text{proj}} = 1$ means that all fibrils are aligned in the flow direction, $S_{\text{proj}} = 0$ is an isotropic system and $S_{\text{proj}} = -0.5$ is a system where all fibrils are aligned normal to the flow direction, shows the same general behaviour: a slight alignment ($0.12 < S_{\text{proj}} < 0.2$) for $x/h < 0$, i.e. in the inlet core flow

https://doi.org/10.1017/flo.2025.8 Published online by Cambridge University Press

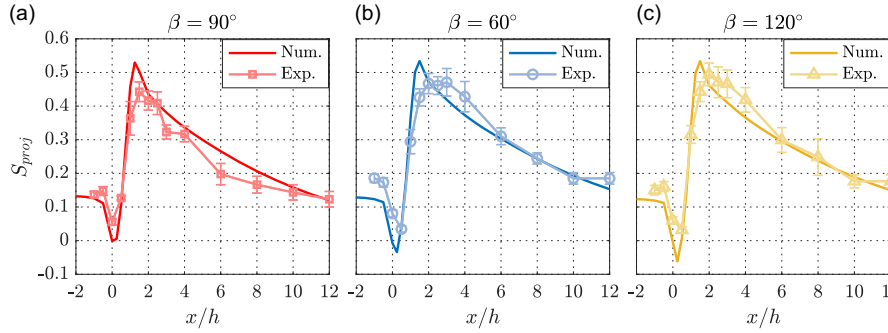

Figure 5. *(a–c) Comparison of simulated (Num.) and measured (Exp.) fibril order (S_{proj}) as a function of downstream x/h positions for three confluence angle ($\beta = 90°, 60°$ and $120°$) geometries. The experimental order parameter is obtained from SAXS measurements, while the simulations are based on equations (2.9)–(2.12) with a two-fraction model. Care is taken to extract the measured quantity (space averaged and projected order parameter) from the simulated data.*

channel. In the confluence region $0 < x/h < 1$, there is first a decrease of alignment followed by a rapid increase to a maximum around 0.5 slightly before and after $x/h = 2$ for the $\beta = 90°$ case (figure 5*a*) and $\beta = (60°, 120°)$ cases (figure 5*b*,*c*), respectively. The numerical alignment model is seen to capture the general behaviour very well, but the full difference between the experimental data in figure 5(*a*) as compared with figure 5(*b*,*c*) is not captured: the simulated curves tend to be above the experiments in figure 5(*a*) and below in figure 5(*b*,*c*). Nevertheless, the simulated alignment captures the experimental observations, including the subtle variations between the different confluence angles, fairly well.

The calibrated alignment model of figure 5 is used to investigate the fibril alignment in the remainder of the paper. It differs somewhat from the model used in Gowda *et al.* (2022). After fitting the model to all three confluence angle ($\beta = 90°, 60°$ and $120°$) geometries, the parameters $D_{r,\text{slow}} = 0.45\ \text{s}^{-1}$, $D_{r,\text{fast}} = 6.4\ \text{s}^{-1}$ and $\alpha_{\text{fast}} = 0.74$ are found to be optimal (i.e. the mean of root-mean-square error is reduced from 0.055 to 0.047 as compared with the parameter values used in Gowda *et al.* (2022)).

3.1.3. Fibril alignment in a wider range of confluence angle geometries

Having seen the two-fraction model capturing the experimental observations of fibril alignment quite well in all the three channel configurations ($\beta = 90°, 60°$ and $120°$), we now utilise the two-fraction model to understand the 3-D fibril orientation states for a wider range of confluence angles (see figure 1*a–e*). In particular, it is shown how the acceleration shown in figure 4*c* affects fibril orientation.

Accordingly, figure 6 shows the quantitative evolution of mean order parameter S, ΔS and $S/\Delta S$ over the cross-sections as a function of downstream x/h positions for different confluence angles β. The black squares (□) on the horizontal axis indicate the streamwise positions of the cross-sectional contours plotted in figure 6(*e*,*f*). From the mean order S in figure 6(*a*), for $x/h \leq 0$, S is almost constant at 0.16 in all cases. At the start of the confluence junction ($x/h > 0$), i.e. right at the entry of the sheath flows, there is a decrease in S for all the configurations as seen from the order distributions in figure 6(*a*) ($x/h = 0.5$). In the $\beta = 30°$ and $\beta = 150°$ geometries, the decrease in S for $0 \leq x/h \leq 1.5$ is larger compared with the other configurations ($\beta = 90°, 60°$ and $120°$), since the deceleration is larger in the two former cases (see figure 4*c*).

Further, after $x/h > 1.00$, as depicted in figure 6(*a*) ($x/h = 1.50, 3.00$), the order continues to increase due to acceleration of the core fluid dispersion generated by the sheath flows, in turn leading to the alignment of fibrils. The highest order of fibril alignment varies among the configurations. As can be seen from the mean order in figure 6(*a*), the peak order for $\beta = (60°, 120°)$ and $\beta = (30°, 150°)$ cases occurs around $x/h \simeq 2$ and $x/h \simeq 2.5$, respectively. Far downstream, $x/h > 3.00$, the order decays for all

https://doi.org/10.1017/flo.2025.8 Published online by Cambridge University Press

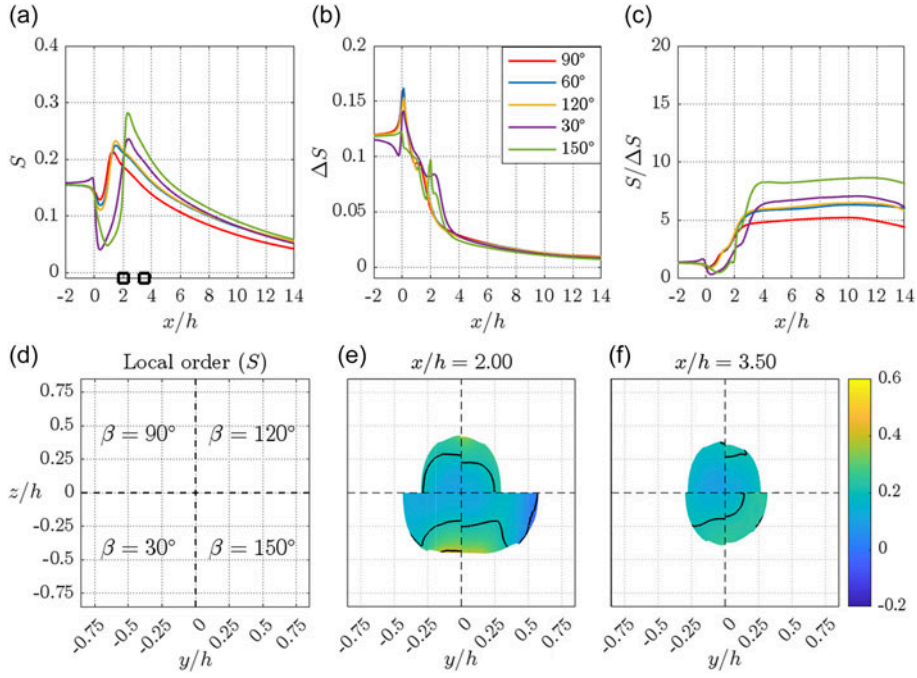

Figure 6. *Streamwise development of mean order parameter S (a), ΔS (b) and $S/\Delta S$ (c) as a function of downstream x/h positions for different confluence angle β geometries. The confluence angle β of each geometrical configuration is indicated in the legend (b). The black square ◘ symbols on the horizontal axis in (a) correspond to the streamwise x/h positions of the cross-sectional contours depicted in (e,f). (d–f) Cross-sectional contours of local order parameter S_{local}, at different streamwise x/h positions. In (e,f), each quarter segment represents different geometrical configurations, and the confluence angle β of each configuration is indicated in (d).*

cases. It is worth noting that the $\beta = 150°$ flow-focusing configuration has higher order and a slower decay far downstream ($x/h > 3$), whereas the standard $\beta = 90°$ flow-focusing configuration has lower maximum order and a more upstream start of the decay ($x/h > 1.75$).

Another important aspect to note from figure 6(*a*) is on the collapse of mean order on top of each other between $\beta = 60°$ and $\beta = 120°$ geometries. The resemblance between these two cases was also seen earlier in the evolution of thread shapes (see figure 4*a*) and strain rate $\dot{\varepsilon}$ along the centreline (see figure 4*c*). On the other hand, the asymmetric behaviour between $\beta = 30°$ and $\beta = 150°$ cases (see figure 4*a*,*c*) is also reflected in the mean order. Also, as seen from figure 6(*c*), $S/\Delta S$, i.e. ratio of alignment to its variation over the cross-section, is smallest for $\beta = 90°$, and the other geometries have a higher degree of alignment and less variation.

Further, figure 6(*e*,*f*) shows the cross-sectional contours of local order at different streamwise x/h positions. In all the flow-focusing configurations, the symmetry along xy and xz planes is exploited, and hence only a quarter of their cross-section is shown. Thus, in figure 6(*e*,*f*), each quarter segment represents a different geometrical configuration, and the confluence angles β are given in figure 6(*d*). As seen from figure 6(*e*,*f*), all the configurations show an increase in the local order parameter towards the edge of the thread. This increased alignment originates from the regions close to the walls of the inlet channel, where the fibril dispersion is exposed to direct shear. This can be noted more clearly from figure 6(*e*) at $x/h = 2.00$.

https://doi.org/10.1017/flo.2025.8 Published online by Cambridge University Press

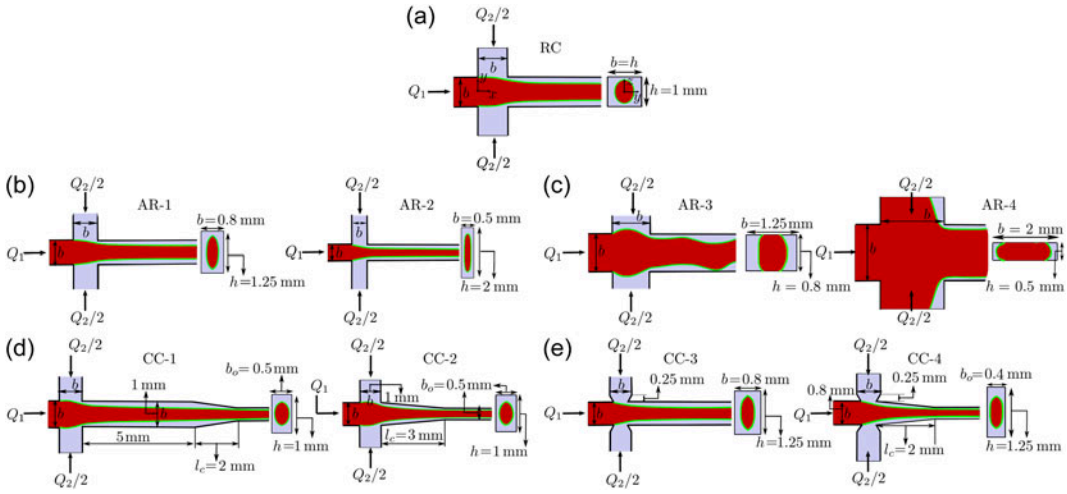

Figure 7. *Illustration of top and cross-sectional views of flow-focusing configurations: (a) RC; (b,c) AR-1 to AR-4; (d,e) CC-1 to CC-4. The cross-sectional width b and height h of all the geometrical configurations are tabulated in table 1.*

3.2. Numerical evaluation of additional geometries

3.2.1. Description of the geometries

Figure 7 shows a schematic illustration of the top and cross-sectional views of the flow-focusing configurations. In total, nine geometrical configurations are investigated. The reference configuration (RC; figure 7*a*) is a channel geometry of confluence angle $\beta = 90^\circ$ with square cross-section of sidelength $h = 1$ mm. All the configurations have four channel arms: one main central channel arm for the core flow inlet, two side-channel arms for the sheath flow inlets and a central outlet channel arm. The channel cross-sectional aspect ratio is defined as $\alpha = b/h$, where b and h are the width and height of the channel arms, respectively.

As seen from figures 7(*a–c*) and 8(*a–c*), the RC and AR-1 to AR-4 configurations have uniform cross-sections with the dimensions of width b and height h as displayed in table 1. The cross-sectional area ($b \times h$) of these configurations remains constant (1 mm^2), whereas the cross-sectional aspect ratio α varies.

In the cases of CC-1 to CC-4 (figures 7*d*,*e* and 8*d*,*e*), converging sections of varying lengths (l_c = 0.25, 2 and 3 mm) are appended after the flow-focusing geometries. All the channel arms of the respective geometries have uniform height h as tabulated in table 1. When it comes to the width b of the channel arms, only the width of the inlet channel arms is uniform, whereas the width b_o of the outlet channel arms varies as shown in figure 7(*d*,*e*). The cross-sectional width b, height h and aspect ratio α of the inlet channel arms for all the configurations are reported in table 1.

Further, in the CC-1 case, a converging section of length $l_c = 2$ mm starts at $x/h = 5$, while, in the CC-2 case, a converging section of length $l_c = 3$ mm begins right at the end of focusing region at $x/h = 1$. In both CC-1 and CC-2 cases, the cross-sectional width b and height h of the inlet channel arms are the same as those of the RC case.

For the CC-3 and CC-4 configurations, the cross-sectional width b and height h of the inlet channel arms are equivalent to those of the AR-1 case. In both the CC-3 and CC-4 cases, the sheath flow inlet channel arms in the y direction have a converging section of length $l_c = 0.25$ mm (figure 7*e*) at the confluence region. In addition, for the CC-4 configuration, a converging section of length $l_c = 2$ mm is added in the streamwise x direction right at the end ($x/h = 1$) of the focusing region.

https://doi.org/10.1017/flo.2025.8 Published online by Cambridge University Press

Table 1. *Cross-sectional width b, height h and aspect ratio α of the flow-focusing geometries illustrated in figure 7. The inlet channel of all the geometries has the same cross-sectional area $b \times h = 1\ mm^2$. The details of the thread features, namely the wetted length L_w/h, thread aspect ratio $\varepsilon_z/\varepsilon_y$, maximum Ar_{max} and final Ar_{final}, displayed in figures 9 and 10 are also tabulated.*

Case	b (mm)	h (mm)	$\alpha = b/h$	L_w/h	Ar_{max} (☆)	Ar_{final} (★)
RC	1	1	1	2.10	1.68	1.60
AR-1	0.8	1.25	1.56	0.83	2.30	2.00
AR-2	0.5	2	4	0.27	7.75	6.06
AR-3	1.25	0.8	0.64	∞	–	–
AR-4	2	0.5	0.25	∞	–	–
CC-1	1	1	1	2.10	1.75	1.65
CC-2	1	1	1	1.57	2.03	1.90
CC-3	0.8	1.25	1.56	0.65	2.53	2.27
CC-4	0.8	1.25	1.56	0.61	3.07	2.77

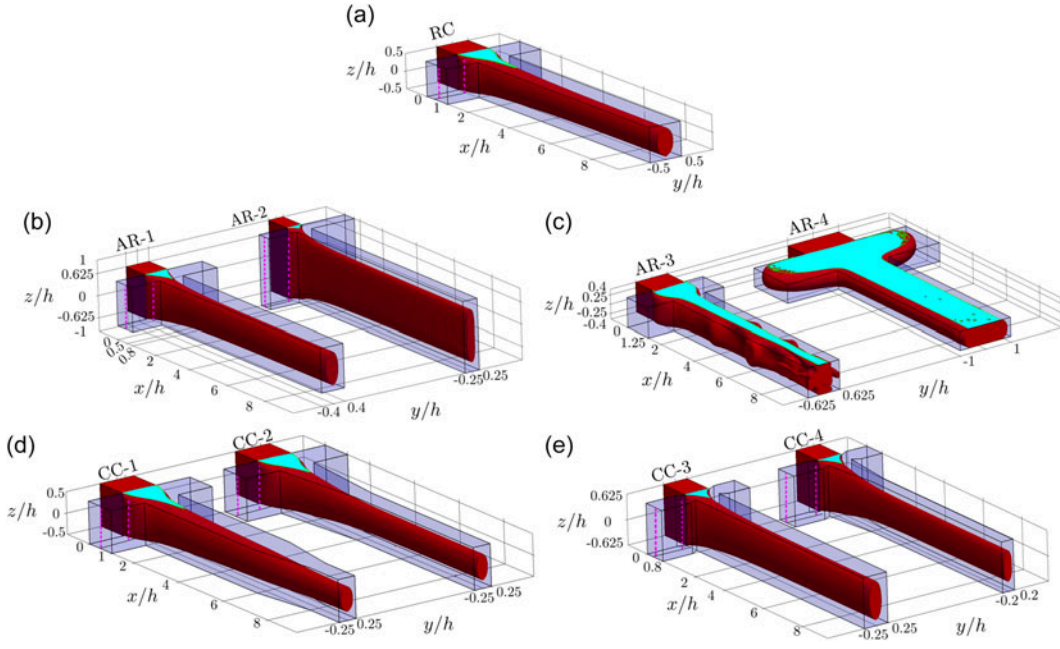

Figure 8. *Three-dimensional views of the thread shapes in various flow-focusing geometries: (a) RC; (b,c) AR-1 to AR-4; (d,e) CC-1 to CC- 4. The aqua colour zone at the top plane in all the geometries indicates the region wetted by the core fluid dispersion before detachment. In (c), the aqua colour extends all along the channel length in the x direction indicating the core fluid dispersion never detaches from the top and bottom channel walls. The dashed magenta vertical lines along the centre of side channels in the z direction denote the upstream and downstream y/h positions of the velocity profiles plotted in figure 9.*

https://doi.org/10.1017/flo.2025.8 Published online by Cambridge University Press

3.2.2. Thread shapes

Figure 8 shows the 3-D shape of the core fluid thread for all the nine configurations. The aqua colour at the top plane of the respective geometry indicates the region wetted by the core fluid dispersion before the detachment from the top and bottom channel walls. Depending on the cross-sectional aspect ratio α of the channel arms (see table 1), thread shapes vary.

For the AR-1 and AR-2 cases, where $\alpha > 1$, the threads are thinner, and the wetted regions are shorter as compared with the RC ($\alpha = 1$) case. On the other hand, for the AR-3 and AR-4 cases, where $\alpha = 1$, the core fluid remains attached to the top and bottom channel walls (indicated by aqua colour) all along the outlet channel length, and eventually develops instabilities far downstream. For CC-1 to CC-4, where $\alpha \geq 1$, figure 8(*d*,*e*) shows that the effect of converging sections appears to impact both the thread shape and wetted regions.

In order to comprehend the variations in the thread features among all the configurations, a quantitative analysis is carried out utilising the sheath flow velocity profiles, wetted lengths L_w/h and the thread aspect ratio $\varepsilon_z/\varepsilon_y$ as detailed below. Besides, as the flow is unstable in the AR-3 and AR-4 configurations, these two cases are excluded from the following analysis.

3.2.3. Velocity profiles and wetted length

Figure 9 shows the sheath flow velocity profiles as a function of normalised channel height ($z/z_{\max}$) at different y/h locations (upstream and downstream as indicated by dashed magenta lines in figure 8) together with the wetted region shapes for all the geometrical configurations. Note that U represents the velocity magnitude in the x direction. In all the cases, the upstream location is near the sheath flow inlet after the flow is fully developed, and the downstream position is near the focusing region.

As seen from figure 9(*a*), the upstream sheath flow velocity profile is parabolic in both RC and AR-1 (aspect ratio $\alpha = 1$ and 1.56) cases, while in the AR-2 case, the profile exhibits a plug-flow-like behaviour due to the higher aspect ratio ($\alpha = 4$) of the sheath flow channel arms. Further downstream, as observed in figure 9(*b*), the profiles in RC and AR-1 cases display more or less parabolic shapes with a slightly higher magnitude in the AR-1 case. In the case of AR-2, the velocity profile is uniform for most of the channel height except closer to the channel walls where the velocity is high.

The downstream sheath flow velocity profiles influence the core fluid thread detachment, i.e. the wetted lengths L_w/h, as depicted in figure 9(*c*). The plug-flow profile in the AR-2 case leads to an early detachment of the core fluid thread from the top and bottom channel walls, leading to a shorter $L_w/h \simeq 0.27$, compared with AR-1 ($L_w/h \simeq 0.83$) and RC ($L_w/h \simeq 2.1$) cases. All the values of L_w/h in the different cases are tabulated in table 1.

Continuing to the upstream velocity profiles of the sheath flow in RC and CC-1 to CC-4 cases, as seen from figure 9(*d*), the velocity profiles are parabolic. At this point, it is worth recalling that the aspect ratio α of the inlet channel arms of CC-1 and CC-2 cases is the same as that of the RC case ($\alpha = 1$), while that of CC-3 and CC-4 cases corresponds to that of the AR-1 ($\alpha = 1.56$) case.

At the downstream position (figure 9*e*), the velocity profiles of CC-1 and RC cases overlap each other as expected, since both configurations have the same α, and as such, there is no influence of the converging section, which is 5 mm downstream from the confluence region. Also, the wetted length L_w/h (figure 9*f*, $L_w/h \simeq 2.1$) is the same, with and without the converging section. However, in the CC-2 case, the converging section begins right at the end of the confluence region $x/h = 1$. Also here, the velocity profiles (figure 9*e*) overlap with the RC case, but the wetted length L_w/h (see figure 9*f*) in the CC-2 case ($L_w/h \simeq 1.5$) is shorter than that in the RC case ($L_w/h \simeq 2.1$). This difference in L_w/h could be attributed to the converging section.

On the other hand, figure 9(*e*,*f*) shows that in cases CC-3 and CC-4, both velocity profiles and the wetted regions almost collapse on top of each other. The uniqueness of these two configurations is with regard to the velocity profiles. Both have the same cross-sectional aspect ratio ($\alpha = 1.56$) of the sheath flow inlet channel arms, which is similar to the AR-1 case, but exhibit plug-flow-like flow profiles as observed in the high-aspect-ratio ($\alpha = 4$) AR-2 configuration (figure 9*b*). This, in turn, leads to an early

https://doi.org/10.1017/flo.2025.8 Published online by Cambridge University Press

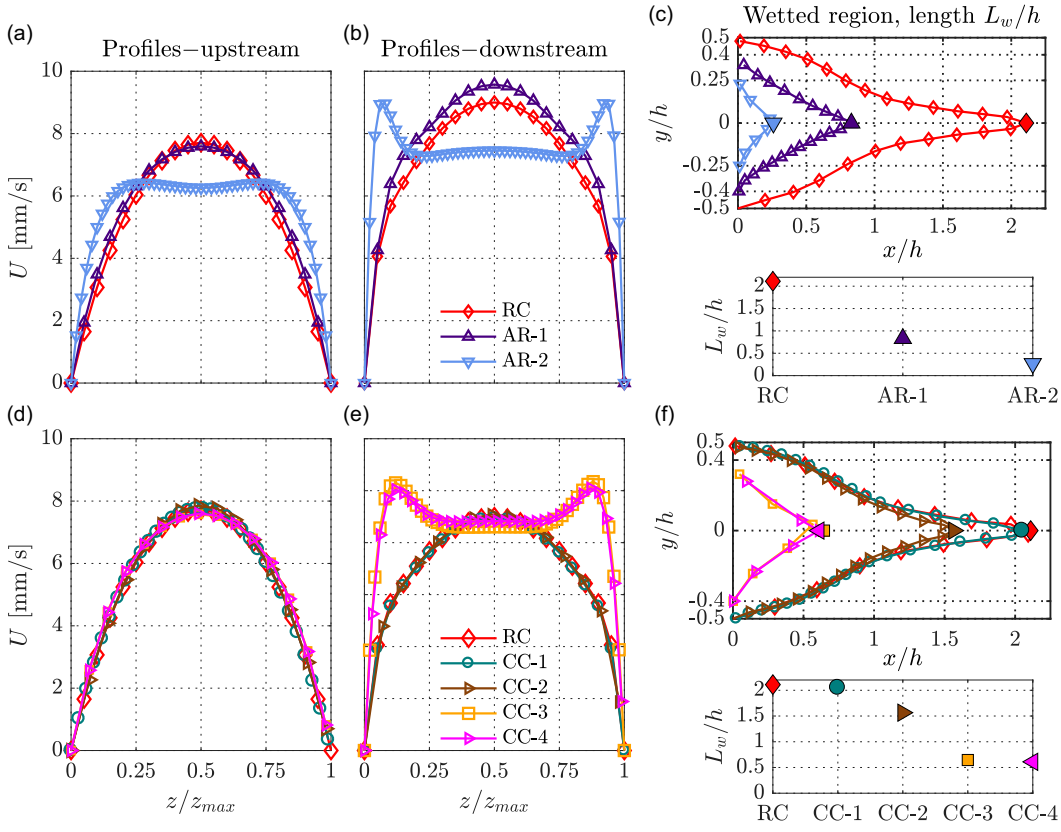

Figure 9. *(a–c) Cases RC, AR-1 and AR-2; (d–f) RC, CC-1 to CC-4. Sheath flow velocity profiles as a function of normalised channel height (z/z_{max}) at upstream (a,d) and downstream (b,e) y/h locations (indicated by dashed magenta lines in figure 8). In (c,f), the top rows show the wetted region morphologies. The filled symbols in both top and bottom rows depict the wetted lengths (L_w/h) of respective geometrical configurations.*

detachment of the core fluid thread with shorter wetted lengths $L_w/h \simeq 0.65$ and 0.61 (see figure 9*f*) compared with $L_w/h \simeq 0.83$ for the AR-1 case (see figure 9*c*). Indeed, this behaviour in both AR-1 and AR-2 configurations could be attributed to the converging sections at the end of the sheath flow inlet channel arms. Meanwhile, the converging section in the core flow inlet channel arm in the CC-4 case could also play a role to some extent, similar to the case of CC-2 resulting in a slightly shorter $L_w/h \simeq 0.61$ compared with $L_w/h \simeq 0.65$ for the CC-3 case.

Thus, having understood the velocity profiles and wetted lengths of all geometrical configurations, we now examine other aspects such as development of thread aspect ratio $\varepsilon_z/\varepsilon_y$ and strain rate $\dot{\varepsilon}$ along the centreline.

3.2.4. Thread aspect ratio and strain rate

Figure 10 shows the normalised thread aspect ratio ($\varepsilon_z/\varepsilon_y$) and strain rate ($\dot{\varepsilon} = \partial u/\partial x$) along the centreline as a function of downstream x/h positions together with the maximum ($Ar_{\max}$) and final (Ar_{final}) aspect ratio of the threads. In figure 10(*a*,*d*), all the thread aspect ratios $\varepsilon_z/\varepsilon_y$ are normalised with the corresponding inlet channel arm cross-sectional aspect ratio α (see table 1). Thus, the thread aspect ratios $\varepsilon_z/\varepsilon_y$ plotted in figure 10(*a*,*d*) for cases AR-1, AR-2, CC-3 and CC-4 are much higher than for the RC case. In figure 10(*b*,*e*), $Ar_{\max}$ and Ar_{final} represent the actual values.

https://doi.org/10.1017/flo.2025.8 Published online by Cambridge University Press

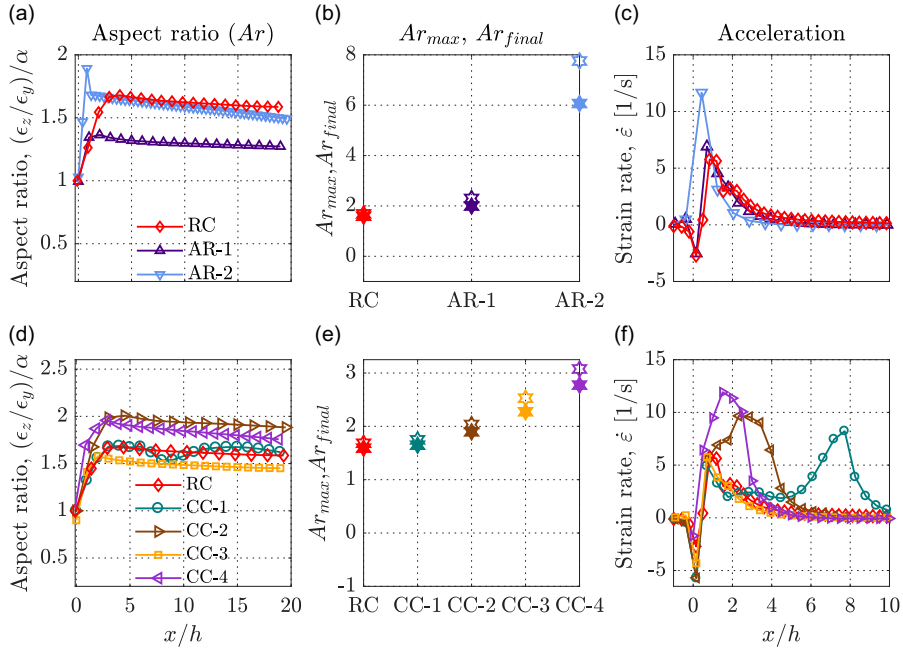

Figure 10. *(a–c) Cases RC, AR-1 and AR-2; (d–f) RC, CC-1 to CC-4. (a,d) Evolution of thread aspect ratio (ϵ_z/ϵ_y) (normalised with the inlet channel arm cross-sectional aspect ratio α; table 1) as a function of downstream x/h positions. (b,e) The maximum (Ar_{max}, open ☆ symbols) and final (Ar_{final}, filled ★ symbols) thread aspect ratio $\varepsilon_z/\varepsilon_y$ for all the geometries. (c,f) Evolution of strain rate $\dot{\varepsilon}$ along the centreline as a function of downstream positions x/h.*

A closer view of figure 10(*a*) shows that the thread aspect ratio $\varepsilon_z/\varepsilon_y$ increases in RC, AR-1 and AR-2 cases until the position of thread detachment (see figure 9*c* or table 1). Thereafter, the thread shape remains more or less constant. In fact, depending on the channel arm cross-sectional aspect ratio α (table 1), the cross-sectional shapes of the thread vary. As observed from figure 10(*b*), $Ar_{\max}$ and Ar_{final} are highest for the slender channel (AR-2), followed by the AR-1 and RC cases. In all the configurations, Ar_{final} is the mean value of $\varepsilon_z/\varepsilon_y$ for $15 \leq x/h \leq 20$.

The variation in strain rate $\dot{\varepsilon}$ along the centreline in figure 10(*c*) follows a pattern similar to $Ar_{\max}$ and Ar_{final}. The strain rate $\dot{\varepsilon}$ is higher for the slender thread (AR-2 case) compared with AR-1 and RC cases. However, it is important to note that the length of the region where $\dot{\varepsilon} > 0$ is the shortest ($0 \leq x/h \leq 2$) for the AR-2 case, while it is more or less similar ($0 \leq x/h \leq 4$) for AR-1 and RC cases.

Turning to the configurations with converging sections, CC-1 to CC-4 cases, figure 10(*d*) shows that in the case of CC-1, the thread aspect ratio $\varepsilon_z/\varepsilon_y$ dips for $6 \leq x/h \leq 8$. In the CC-2 configuration, the combined effects of sheath flow momentum ($0 \leq x/h \leq 1$) and the converging section ($1 \leq x/h \leq 3$) result in a more pronounced development of the thread with higher $\varepsilon_z/\varepsilon_y$. As seen from figure 10(*e*), although $\alpha = 1$ remains the same in RC, CC-1 and CC-2 cases, the converging sections in CC-1 and CC-2 cases produce higher $Ar_{\max}$ and Ar_{final} than in the RC case. In fact, the strain rate $\dot{\varepsilon}$ along the centreline in figure 10(*f*) shows a clear impact of the converging sections, wherein, for the CC-1 case, $\dot{\varepsilon}$ shoots up for $6 \leq x/h \leq 8$, and in the CC-2 case, $\dot{\varepsilon} > 0$ extends from $x/h = 0$ all the way up to $x/h = 5$.

Additionally, in the CC-3 and CC-4 cases, $Ar_{\max}$ and Ar_{final} (figure 10*e*) are much higher than in RC, CC-1 and CC-3. It is worth recalling that CC-3 and CC-4 are the modified channel configurations with $\alpha = 1.56$, which is the same as AR-1. In comparison with AR-1 (figure 10*b*,*c*), the effect of the converging section in the sheath flow inlet in CC-3 appears to be small with a minor increment in $Ar_{\max}$, Ar_{final} and strain rate $\dot{\varepsilon}$. However, the effect on wetted length L_w/h was substantial (see figure 9*f*).

https://doi.org/10.1017/flo.2025.8 Published online by Cambridge University Press

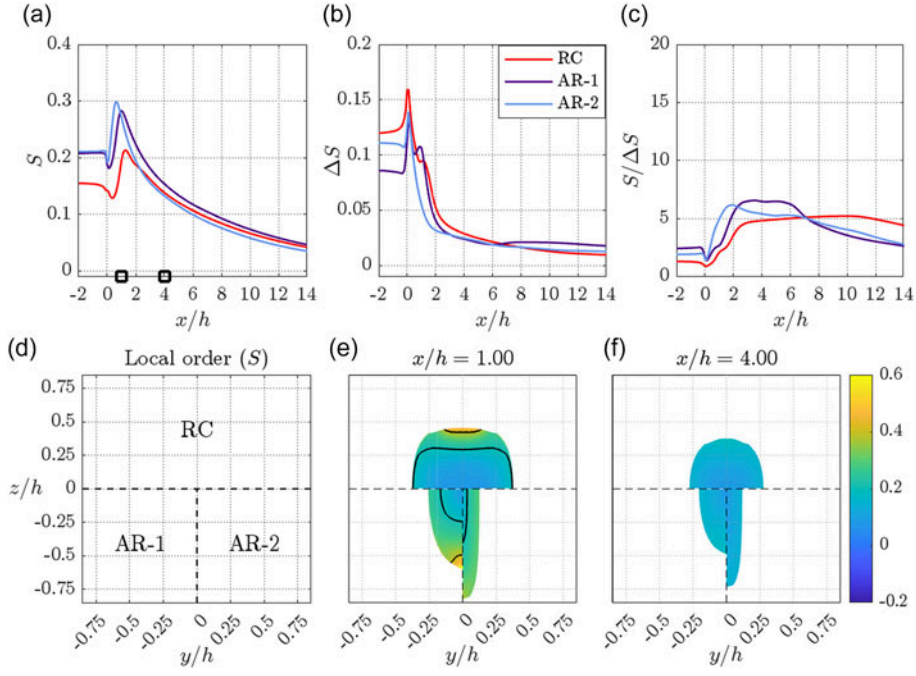

Figure 11. *(a–c) Streamwise development of mean order parameter S (a), ΔS (b) and S/ΔS (c) as a function of downstream x/h positions for RC, AR-1 and AR-2 geometries. The black square ◘ symbols on the horizontal axis in (a) correspond to the streamwise x/h positions of the cross-sectional contours depicted in (e,f). (d–f) Cross-sectional contours of local order parameter S_{local}, at different streamwise x/h positions. As indicated in (d), in (e,f), the top-half segment represents the RC case and the bottom half represents AR-1 and AR-2 cases.*

Addition of a converging section downstream of the confluence region in the streamwise x direction, as in the case of CC-4, brings in a substantial increase in $Ar_{\max}$ and Ar_{final} of the thread aspect ratio and the strain rate $\dot{\varepsilon}$ as depicted in figure 10(*e*,*f*).

Summing up, from the thread detachment or wetted length L_w/h point of view, the AR-2 configuration with the channel cross-sectional aspect ratio of $\alpha = 4$ is the ideal choice, since $L_w/h \simeq 0.25$ is the shortest. However, from the alignment of nanofibrils perspective, the narrow or smaller length of the strain rate $\dot{\varepsilon}$ region in AR-2 geometry could plausibly make it less effective. Therefore, from a break-even point of view, i.e. for achieving the shortest wetted length L_w/h and a wider or longer extent of the strain rate $\dot{\varepsilon}$ region, CC-4 would be a near-optimal choice. Adjusting the length of the converging section (l_c) in the streamwise x direction, the strain rate $\dot{\varepsilon}$ region could be expanded to longer lengths in the CC-4 configuration as well.

3.2.5. Simulated nanofibril alignment in the additional geometries

Finally, the fibril alignment in the six geometries of figure 8 is studied numerically. The results are presented in figures 11 and 12 for the AR and CC geometries, respectively. In both figures, panel (*a*) shows streamwise development of the mean order parameter S, panel (*b*) the variance of the local order parameter over the cross-section ΔS and panel (*c*) $S/\Delta S$, i.e. the ratio between alignment and its variation over the cross-section. Again, a high value of $S/\Delta S$ typically indicates a high degree of alignment with limited variation over the cross-section. In panels (*e*) and (*f*), the distribution of the local order parameter over the cross-section is shown with one geometry per quadrant as indicated in panel (*d*). A first observation

https://doi.org/10.1017/flo.2025.8 Published online by Cambridge University Press

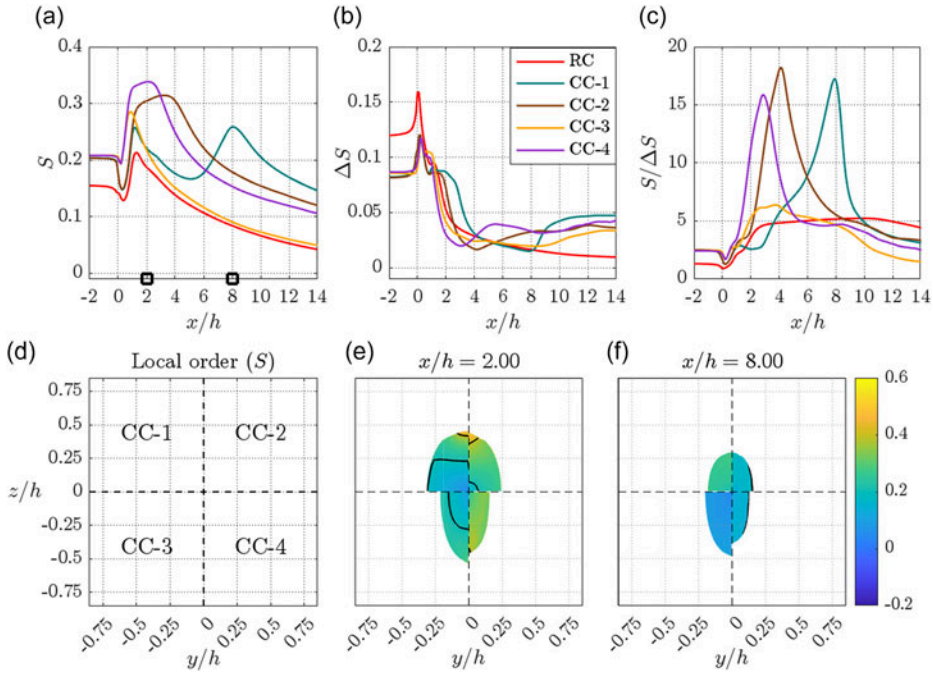

Figure 12. *(a–c) Streamwise development of mean order parameter S (a), ΔS (b) and $S/\Delta S$ (c) as a function of downstream x/h positions for RC and CC-1 to CC-4 geometries. The black square ◘ symbols on the horizontal axis in (a) correspond to the streamwise x/h positions of the cross sectional contours depicted in (e,f). (d–f) Cross-sectional contours of local order parameter S_{local}, at different streamwise x/h positions. In (e,f), each quarter segment represents different geometrical cases of CC-1 to CC-4 as indicated in (d).*

is expected, namely that the alignment development in figures 12(*a*) and 11(*a*) is explained by the strain rate $\dot{\varepsilon}$ development shown in figure 10(*c*,*f*).

The AR geometries (figure 11) are seen to give a slightly higher maximum alignment and similar variation ΔS as compared to RC ($\beta = 90°$). The differences, both with respect to the RC and between the geometries, are more pronounced for the CC geometries shown in figure 12. Compared with RC, the CC geometries produce higher maximum alignment with very small variation over the cross-section, in particular for CC-1, CC-2 and CC-4. The streamwise position of the maximum of $S/\Delta S$ varies and it is clear that the geometry can be designed to deliver high alignment at a certain position. This is of great interest in assembly application, where chemical reactions locking the aligned structure (e.g. pH-controlled gelation or light-induced polymerisation) could be tuned to act at the position of highest alignment.

The alignment results in terms of $S_{\max}$ and $S_{\max}/\Delta S$ for all geometries are summarised in figure 13. The preferred situation, high alignment with small variation, corresponds to the upper-right corner. The importance of contractions is again very clear, since the previously identified CC-1, CC-2 and CC-4 stand out from the other geometries. It is also worth noting that all geometries perform better than RC ($\beta = 90°$).

4. Conclusions

Building on previous combined experimental and numerical method development, the flow and fibril alignment in 11 different flow geometries have been studied. It was demonstrated how the flow geometry

https://doi.org/10.1017/flo.2025.8 Published online by Cambridge University Press

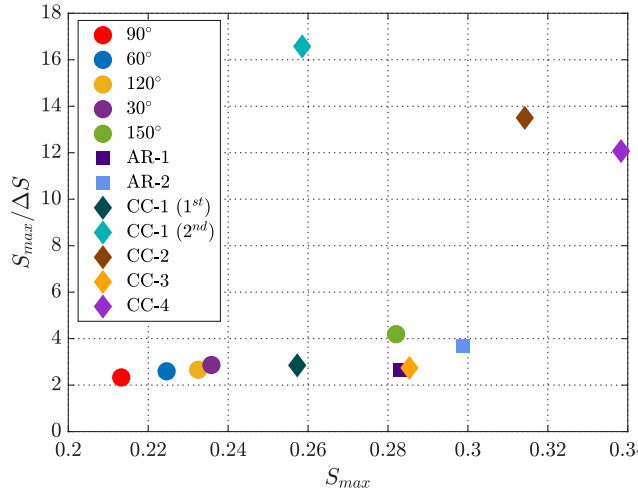

Figure 13. *Peak value of the mean order S_{max} (horizontal axis) and the order homogeneity measure $S_{max}/\Delta S$ (vertical axis) for all geometries as defined in the legend.*

can be used to control thread detachment or wetted length L_w/h, thread aspect ratio $\varepsilon_z/\varepsilon_y$ and fibril alignment. The work is motivated by a desire to understand and control the assembly of nanostructured material in micrometre- and millimetre-sized flow systems.

First, the orientation (or alignment) modelling was seen to be able to capture some, but not all, of the differences in SAXS measurements in flow-focusing geometries with confluence angle $\beta = 90°$, 60° and 120°. Based on the numerical results, it could be concluded that the alignment behaviour varies much more between the other geometries. As expected, the geometries with a contraction in the outlet channel (CC-1, CC-2 and CC-4; see figure 8) generate high alignment with a small variation over the cross-section.

In flow-focusing spinning, thread formation in the channel is critical. In this context, it was demonstrated that a short contraction in the side-flow channels immediately before the confluence region is an efficient means to promote thread detachment from the top and bottom channel walls. This is achieved as a result of the plug-like velocity profiles that are generated by the contractions, with high-momentum side flows close to the top and bottom walls. This high momentum increases the ability of the side flows with low-viscosity fluid to engulf the core flow of high-viscosity fluid.

In a wider perspective, the present work paves the way for optimising the flow geometries for tailored assembly of macroscopic materials from anisotropic nanoscale building blocks.

Data availability. Data are available upon request from the corresponding author.

Author contributions. K.O.: conceptualisation, orientation simulations, writing; V.K.G.: conceptualisation, flow simulations, X-ray experiments, writing; T.R.: X-ray experiments, editing; S.V.R.: X-ray experiments, editing; L.D.S.: supervision, editing; J.S.: editing, supervision; F.L.: conceptualisation, orientation simulations, X-ray experiments, writing, supervision.

Funding. Financial support from FORMAS (the Swedish Research Council for Sustainable Development), the Swedish Energy Agency, the Swedish Research Council, Knut and Alice Wallenberg Foundation via Wallenberg Wood Science Center and the JST Adopting Sustainable Partnerships for Innovative Research Ecosystem (ASPIRE) programme (grant number JPMJAP2310) is gratefully acknowledged. Computational resources were provided by National Academic Infrastructure for Supercomputing in Sweden (NAISS).

Competing interests. The authors declare no conflict of interest.

Ethical standards. The research meets all ethical guidelines, including adherence to the legal requirements of the study country.

https://doi.org/10.1017/flo.2025.8 Published online by Cambridge University Press

References

Anna, S. L., Bontoux, N., & Stone, H. A. (2003). Formation of dispersions using "flow focusing" in microchannels. *Applied Physics Letters*, *82*(3), 364–366.

Atencia, J., & Beebe, D. J. (2005). Controlled microfluidic interfaces. *Nature*, *437*(7059), 648–655.

Brackbill, J. U., Kothe, D. B., & Zemach, C. (1992). A continuum method for modeling surface tension. *Journal of Computational Physics*, *100*(2), 335–354.

Brouzet, C., Mittal, N., Söderberg, L. D., & Lundell, F. (2018). Size-dependent orientational dynamics of brownian nanorods. *ACS Macro Letters*, *7*(8), 1022–1027.

Buffet, A., Rothkirch, A., Döhrmann, R., Körstgens, V., Abul Kashem, M. M., Perlich, J., Herzog, G., Schwartzkopf, M., Gehrke, R., Müller-Buschbaum, P., & Roth, S. V. (2012). P03, the microfocus and nanofocus X-ray scattering (MiNaXS) beamline of the PETRA III storage ring: The microfocus endstation. *Journal of Synchrotron Radiation*, *19*(4), 647–653.

Calabrese, V., Shen, A. Q., & Haward, S. J. (2023). Naturally derived colloidal rods in microfluidic flows. *Biomicrofluidics*, *17*(2), 021301.

Capadona, J. R., Van Den Berg, O., Capadona, L. A., Schroeter, M., Rowan, S. J., Tyler, D. J., & Weder, C. (2007). A versatile approach for the processing of polymer nanocomposites with self-assembled nanofibre templates. *Nature Nanotechnology*, *2*(12), 765–769.

Carbonaro, A., Savorana, G., Cipelletti, L., Govindarajan, R., & Truzzolillo, D. (2025). Emergence of capillary waves in miscible coflowing fluids. *Physical Review Letters*, *134*(5), 054001.

Doi, M., & Edwards, S. F. (1988). *The theory of polymer dynamics*. vol. 73. Oxford University Press.

Ehrlich, H. (2010). Chitin and collagen as universal and alternative templates in biomineralization. *International Geology Review*, *52*(7-8), 661–699.

Gowda, V. K., Rosén, T., Roth, S. V., Söderberg, L. D., & Lundell, F. (2022). Nanofibril alignment during assembly revealed by an x-ray scattering-based digital twin. *ACS Nano*, *16*(2), 2120–2132.

Gowda, V. K., Rydefalk, C., Söderberg, L. D., & Lundell, F. (2021). Formation of colloidal threads in geometrically varying flow-focusing channels. *Physical Review Fluids*, *6*(11), 114001.

Gowda. V, K., Brouzet, C., Lefranc, T., Söderberg, L. D., & Lundell, F. (2019). Effective interfacial tension in flow-focusing of colloidal dispersions: 3-D numerical simulations and experiments. *Journal of Fluid Mechanics*, *876*, 1052–1076.

Håkansson, K. M. O., Henriksson, I. C., de la Peña Vázquez, C., Kuzmenko, V., Markstedt, K., Enoksson, P., & Gatenholm, P. (2016). Solidification of 3D printed nanofibril hydrogels into functional 3D cellulose structures. *Advanced Materials Technologies*, *1*(7), 1600096.

Håkansson, K. M. O., Fall, A. B., Lundell, F., Yu, S., Krywka, C., Roth, S. V., Santoro, G., Kvick, M., Prahl Wittberg, L., Wågberg, L., & Söderberg, L. D. (2014). Hydrodynamic alignment and assembly of nanofibrils resulting in strong cellulose filaments. *Nature Communications*, *5*(1), 4018.

Hou, X., Zhang, Y. S., Santiago, G. T., Alvarez, M. M., Ribas, J., Jonas, S. J., Weiss, P. S., Andrews, A. M., Aizenberg, J., & Khademhosseini, A. (2017). Interplay between materials and microfluidics. *Nature Reviews Materials*, *2*(5), 1–15.

Humblet-Hua, N., Sagis, L. M. C., & van der Linden, E. (2008). Effects of flow on hen egg white lysozyme (hewl) fibril formation: Length distribution, flexibility, and kinetics. *Journal of Agricultural and Food Chemistry*, *56*(24), 11875–11882.

Iwamoto, S., Isogai, A., & Iwata, T. (2011). Structure and mechanical properties of wet-spun fibers made from natural cellulose nanofibers. *Biomacromolecules*, *12*(3), 831–836.

Jeffery, G. B. (1922). The motion of ellipsoidal particles immersed in a viscous fluid. *Proceedings of the Royal Society of London. Series A, Containing Papers of a Mathematical and Physical Character*, *102*(715), 161–179.

Joseph, D. D., & Renardy, Y. Y. (1993). *Fundamentals of two-fluid dynamics. Part II: lubricated transport, drops and miscible liquids*. Springer.

Kamada, A., Mittal, N., Söderberg, L. D., Ingverud, T., Ohm, W., Roth, S. V., Lundell, F., & Lendel, C. (2017). Flow-assisted assembly of nanostructured protein microfibers. *Proceedings of the National Academy of Sciences*, *114*(6), 1232–1237. arXiv:https://www.pnas.org/content/114/6/1232.full.pdf

Kanso, M. A., Piette, J. H., Hanna, J. A., & Giacomin, A. J. (2020). Coronavirus rotational diffusivity. *Physics of Fluids*, *32*(11), 113101.

Korteweg, D. J. (1901). Sur la forme que prennent les équations du mouvement des fluides si l'on tient compte des forces capillaires causées par des variations de densité. *Archives Neerlandaises des Sciences Exactes et Naturelles*, *6*(1), 1–24.

Lagerwall, J. P. F., Schütz, C., Salajkova, M., Noh, J. H., Hyun Park, J., Scalia, G., & Bergström, L. (2014). Cellulose nanocrystal-based materials: From liquid crystal self-assembly and glass formation to multifunctional thin films. *NPG Asia Materials*, *6*(1), e80.

Li, T., Chen, C., Brozena, A. H., Zhu, J. Y., Xu, L., Driemeier, C., Dai, J., Rojas, O. J., Isogai, A., Wågberg, L., & Hu, L. (2021). Developing fibrillated cellulose as a sustainable technological material. *Nature*, *590*(7844), 47–56.

Ling, S., Kaplan, D. L., & Buehler, M. J. (2018). Nanofibrils in nature and materials engineering. *Nature Reviews Materials*, *3*(4), 1–15.

Ling, S., Qin, Z., Li, C., Huang, W., Kaplan, D. L., & Buehler, M. J. (2017). Polymorphic regenerated silk fibers assembled through bioinspired spinning. *Nature Communications*, *8*(1), 1387.

https://doi.org/10.1017/flo.2025.8 Published online by Cambridge University Press

Loveday, S. M., Su, J., Rao, M. A., Anema, S. G., & Singh, H. (2012). Whey protein nanofibrils: Kinetic, rheological and morphological effects of group IA and IIA cations. *International Dairy Journal*, *26*(2), 133–140.

Hyensjö, M., & Dahlkild, A. (2008). Study of the rotational diffusivity coefficient of fibres in planar contracting flows with varying turbulence levels. *International Journal of Multiphase Flow*, *34*(9), 894–903.

Mittal, N., Ansari, F., Gowda, K., Brouzet, C., Chen, P., Larsson, P. T., Roth, S. V., Lundell, F., Wågberg, L., Kotov, N. A., & Söderberg, L. D. (2018). Multiscale control of nanocellulose assembly: Transferring remarkable nanoscale fibril mechanics to macroscale fibers. *ACS Nano*, *12*(7), 6378–6388.

Moon, R. J., Martini, A., Nairn, J., Simonsen, J., & Youngblood, J. (2011). Cellulose nanomaterials review: Structure, properties and nanocomposites. *Chemical Society Reviews*, *40*(7), 3941–3994.

Nemoto, N., Schrag, J. L., Ferry, J. D., & Fulton, R. W. (1975). Infinite-dilution viscoelastic properties of tobacco mosaic virus. *Biopolymers: Original Research on Biomolecules*, *14*(2), 409–417.

Nunes, J. K., Tsai, S. S. H., Wan, J., & Stone, H. A. (2013). Dripping and jetting in microfluidic multiphase flows applied to particle and fibre synthesis. *Journal of Physics D: Applied Physics*, *46*(11), 114002.

Solomon, M. J., & Spicer, P. T. (2010). Microstructural regimes of colloidal rod suspensions, gels, and glasses. *Soft Matter*, *6*(7), 1391–1400.

Truzzolillo, D., Mora, S., Dupas, C., & Cipelletti, L. (2016). Nonequilibrium interfacial tension in simple and complex fluids. *Physical Review X*, *6*(4), 041057.

Truzzolillo, D., Roger, V., Dupas, C., Mora, S., & Cipelletti, L. (2015). Bulk and interfacial stresses in suspensions of soft and hard colloids. *Journal of Physics: Condensed Matter*, *27*(19), 194103.

Tucker, C. L.III (2022). *Fundamentals of fiber orientation: Description, measurement and prediction*. Carl Hanser Verlag GmbH Co KG.

Van Gurp, M. (1995). The use of rotation matrices in the mathematical description of molecular orientations in polymers. *Colloid and Polymer Science*, *273*(7), 607–625.

Weller, H. G., Tabor, G., Jasak, H., & Fureby, C. (1998). A tensorial approach to computational continuum mechanics using object-oriented techniques. *Computers in Physics*, *12*(6), 620–631.

Cite this article: Osawa K., Krishne Gowda V., Rosén T., Roth S. V., Söderberg L. D., Shiomi J. and Lundell F. (2025). Regulating nanofibril assembly using diverse flow-focusing channels. *Flow*, *5*, E12. https://doi.org/10.1017/flo.2025.8